Journal of Environmental Chemical Engineering 12 (2024) 111595

Contents lists available at ScienceDirect

Journal of Environmental Chemical Engineering

journal homepage: www.elsevier.com/locate/jece

Boosting the photocatalytic performance of PAN-TiO_2 nanostructured membranes by mechanosynthesis

Abhishek Anand [a], Eleonora Aneggi [b], Carlo Boaretti [a], Alessandra Lorenzetti [a], Alessandro Trovarelli [c], Michele Modesti [a], Martina Roso [a,*]

[a] University of Padova, Department of Industrial Engineering, Via Marzolo, 9, 35131 Padova, Italy
[b] University of Udine, Department of Agrifood, Environmental and Animal sciences, via del Cotonificio 108, 33100 Udine, Italy
[c] University of Udine, Polytechnic Department of Engineering and Architecture and INSTM, via del Cotonificio 108, 33100 Udine, Italy

ARTICLE INFO

Editor: Javier Marugan

Keywords:
Mechano-synthesis
Electrospun media
Photocatalysis
Indoor Air Purification
VOCs

ABSTRACT

Mechano-synthesized TiO_2 nanoparticles have been explored for their activity towards gas-phase photodegradation of methanol. The effect of milling time over the photoactivity in terms of degradation efficiency has been studied. Titania nanopowders milled for 2 and 8 h were compared with the commercial unmilled catalyst and it has been established that there is a significant impact of milling time over the activity of the catalyst. The current study unveiled that the 2 hr milled sample performs far superior than the pristine catalyst with several order higher kinetics, while with further increase in the milling time the activity drastically reduces. Such behavior has been attributed to higher absorption of radiation as well as increased photo-carrier generation in the milled samples.

1. Introduction

In these past few decades investigation of indoor and outdoor air quality has become a significant concern. Among air persistent pollutants, Volatile Organic Compounds (VOCs) represent a heterogeneous group of organic chemicals largely utilized in the industrial activities associated with the use of solvents, such as printing, spray painting, etc. Due to the pressing need for actions to improve the air quality and protect people and ecosystems from the threats posed by air pollution, there has been tremendous scientific efforts to investigate the potential strategies for their control and abatement [1,2].

Metal oxide nanostructures, owing to their large specific surface area, have been widely explored for the catalytic treatment of several types of pollutants present in the atmosphere [3,4]. Their exposed surface contributes towards the improved interaction and thus leading to the adsorption of submicron contaminant species which predominantly results in the removal while simultaneously assisting in the surface reactions, if any, for the abatement of organic compounds [5].

Understandably, the activity of catalysts depends on their surface area and in order to utilize their properties in an efficient manner, it is reasonable to employ a nanostructured medium for their immobilization. Electrospinning is a facile technique, which has been extensively explored for the fabrication of nanofibers for numerous potential applications towards environmental sustainability [6] The electrohydrodynamics based process has further been used for the catalytic coating of nanoparticles over electrospun structures in order to obtain multifunctional membranes [7–9]. According to our previous work [10,11] active filter media based on electrospun fibers conveniently coupled with photocatalysts nanoparticles (mainly TiO_2), have been proven to be a promising candidate in the development of advanced solutions for indoor environmental quality improvement by exploiting the photocatalytic processes. The milling process for the preparation of catalytic formulations is considered an ecofriendly method with promising commercial and industrial potential, thanks to its numerous advantages such as easy production, energy efficiency, reduction of reaction times, high yields and minimal or no use of solvents [12,13]. We recently reported that the milling of ceria with carbon soot results in the formation of a CeO_2 core wrapped in a soft carbon shell [14,15]; the nanoscale arrangement created by mixing was promoted by the different hardness of the two materials that helps the spreading of the softer carbon particles on the surface of ceria.

During the milling process, the chemical precursors undergo intense mechanical treatment which allows the synthesis of the desired material by the breaking and formation of the chemical bonds. The mechanical

* Corresponding author.
E-mail address: martina.roso@unipd.it (M. Roso).

https://doi.org/10.1016/j.jece.2023.111595
Received 9 June 2023; Received in revised form 22 September 2023; Accepted 25 November 2023
Available online 28 November 2023

stress imparted during synthesis leads to further deformations of the bond, as well as introducing surface and mass defects, irregularities that can improve overall material properties including the oxygen mobility, which is potentially helpful towards catalytic reactions [16–19].

Among the intervention strategies implemented for enhancing the photocatalytic performance of electrospun active mats, the present work focuses on the application of a mechanochemical method as an interesting, alternative, solvent-free, energy efficient and sustainable route for the preparation of ultra-fine solid nanocrystalline catalytic materials [20]. .

In the current work, mechanosynthesized TiO_2 nanoparticles immobilized over electrospun PAN nanofibrous media have been used for the destructive abatement of methanol as the target VOC. Methanol is profoundly present in the closed space with wooden structure e.g. old wooden house, where decomposition of the building material is the major source of methanol emission [21,22]. While in the modern buildings, where cleaning products are overwhelmingly used, thus further contributing to increase in indoor methanol concentration [23, 24]. In reality, methanol is the most abundant non-methane VOC present in the atmosphere [25]. .

2. Experimental section

2.1. Materials

Titanium dioxide nanoparticles (Aeroxide P25, Evonik Industries), with 99.5% purity, has been used as the reference throughout the study. N,N-Dimethylformamide (DMF) and Ethanol have been obtained from Sigma-Aldrich. Dynasylan-4144 (Evonik Industries) was used as the dispersant for the nanoparticles. The polymer polyacrylonitrile (PAN) (M_w = 150,000 Da) was purchased from Sigma-Aldrich, and has been used as the immobilization media for all three catalytic systems. Milli-Q ultrapure water has been used during the preparation of catalyst suspensions.

The as-procured commercial P25 was milled at 50 Hz in a mill (Pulveristte 23, Fritsch) using ZrO_2 vials (volume of the zirconia bowl-15 ml) and one zirconia ball (diameter = 15 mm; weight =10 g; ball-to-powder ratio (BPR)= 10) for durations of 2 h and 8 h and from hereon, they have been designated as P25–2 h and P25–8 h, respectively.

2.2. Preparation of the photoactive media

The photoactive membranes have been prepared by electrohydrodynamics processes i.e. electrospinning of PAN followed by electrospraying of catalysts over the as-prepared membrane, in step-by-step fashion.

6 ml of 5% PAN solution in DMF has been prepared by overnight stirring at 40 °C for each system. The as-prepared solution was electrospun using a lab-scale electrospinning setup with the solution being pumped at 1 ml/hr through a metallic capillary (0.42 mm diameter), connected to a DC voltage source and supplied with 10 kV of positive potential. The fibers were collected over a metallic drum collector, rotating at 500 rpm. Prior to electrospinning, the collector surface was covered with commercial fiberglass mesh with an area of 270 cm^2, which acts as a mechanical support for the electrospun membrane without any significant pressure drop during subsequent experiments. The fiber deposition was carried out under the ambient conditions maintained at 27 °C and 40% relative humidity. The same procedure has been carried out for all other systems.

The suspensions containing catalyst nanoparticles were prepared by mixing 1 g of catalyst with 17 g binary solvent system comprising of Milli-Q and ethanol in the ratio 2.4:1. The mixing was done initially for 1 h using ultrasonic bath and 1 wt% of the dispersant Dynasylan-4144 was added to the suspension. It was followed by 1 h of ultrasonic probe assisted sonication while the temperature was maintained during the whole process. After overnight drying of the prepared membranes, electrospraying of catalytic suspensions were carried out in a controlled environment. The obtained membranes coated with respective catalysts, then, kept overnight again in the oven for the removal of any remnant solvent and have been used afterwards for the following photocatalytic experiments.

2.3. Characterization

Textural characteristics of all samples were measured according to the BET method by nitrogen adsorption at −196 °C, using a Tristar 3000 gas adsorption analyser (Micromeritics). Preliminary crystallographic characterizations of the catalysts have been carried out using an X-ray diffractometer (Panalytical X'Pert 3 powder) with copper radiation (Cu Kα, λ = 1.54 Å) at 50 kV and 40 mA source in the range 0–85°. The degree of crystallinity has been obtained using Eq. 1, where A_c is the area of crystalline diffraction peak while A_t is the total Area of all the diffraction peaks including crystalline as well as amorphous regions.

$$Degree \quad of \quad Crystallinity = \frac{A_c}{A_t} x100 \tag{1}$$

While, for determination of the average crystallite size (D), Scherrer's equation has been used (equ. 2), where K (0.9) is the Scherrer's constant, λ is the wavelength of X-ray (0.15406 nm), ß is the full width at half maximum, and Θ is the diffraction angle.

$$D = \frac{K\lambda}{ßCos\Theta} \tag{2}$$

Rietveld refinement [26] of the XRD pattern was performed by means of a GSAS-EXPGUI program [27,28].

The morphological information of the catalysts has been obtained using a scanning electron microscope (SEM) JSM 6490 (Jeol Ltd.) after sputter coating the samples to a thickness of 5 nm of Au. Transmission Electron Microscope (TEM) images of the catalysts have been collected with FEI, TEM (Tecnai G2) equipped with a side-mounted camera (Olympus Veleta) and a bottom-mounted camera (TVIPS F114), after drop casting the samples on copper grids. Fourier transform infrared spectroscopy (FTIR) of the powdered samples have been performed using Nicolet iS50 spectrometer (Thermo Fisher Scientific), working in the absorbance mode. The average catalytic content and distribution uniformity was obtained by thermogravimetric analysis (TGA) of the membranes performed in air atmosphere by Q600 (TA Instruments), as the temperature was raised from the ambient to 850 °C with a heating rate of 20 °C min^{-1}.

2.4. Photocatalytic activity

The as-obtained membrane after the addition of another fiberglass mesh, so as to create a sandwiched structure, has been installed in a lab-made tubular plug flow reactor with the catalyst coated surface facing the excitation source. The basic reactor setup has been schematically shown in the Fig. 1(b), whereas a detailed representation has been provided in Fig. S1. The photoreactor has a provision for injecting the UV lamp annularly by means of an already installed quartz tube, acting as a medium to transfer the UV irradiation while maintaining the closed state of reaction environment. A fixed amount of the pollutant (methanol) has been placed in an Arnold cell maintained at 0 °C, which when connected to the air tank, is able to supply the desired concentration of methanol vapor to the reaction environment. The qualitative/quantitative analysis of the species present in the reaction environment have been carried out using a gas chromatography coupled with mass spectrometry instrument (GC- Trace 1300, MS- ISQ QD, Thermo Scientific Inc.). A fused silica capillary column (MEGA 1) has been used (30 m x 0.32 mm × 0.15 μm) has been used for the chromatography, while the temperature was held at 60 °C for 5 min followed by heating at 20 °C/min to 250 °C for 3 min. The samples were injected with a 1000 μL gas syringe at a time-interval of 20 min through a six-port external-injection

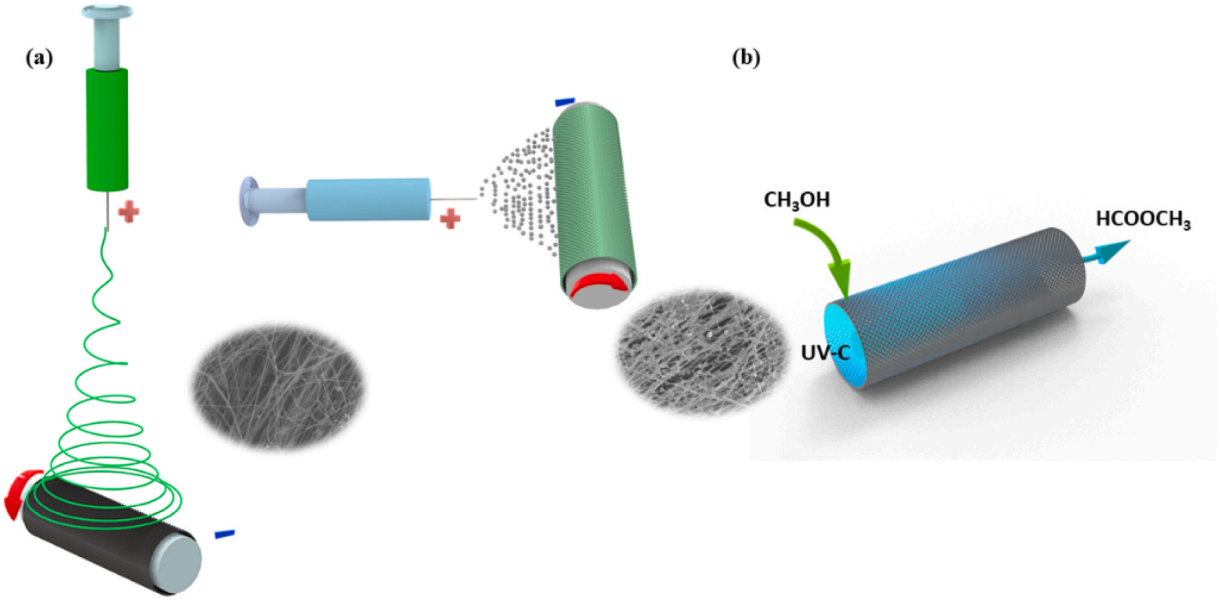

Fig. 1. Schematics of (a) Membrane fabrication steps in order, (b) Reactor setup.

GC valve (6890, Valco Instrument Co., Inc., USA) with a 500 μL sample loop into a HP G1800C GCD series II gas chromatograph/mass spectrometer with pure helium as the carrier gas. A detailed description of the procedure can be found in the Supporting information file. (S1).

The reactor has been designed to work in continuous as well as the batch mode and for the current studies, the latter configuration has been used. After obtaining the steady state conditions in the continuous mode, the reactor is switched to the batch type with recycling. The UV lamp (254 nm, Light Progress) was turned on, once the reaction conditions had been stabilized, and the samples were taken and analyzed by GC/MS at regular time intervals. A blank test has also been performed to find the potential degradation of methanol under the UV irradiation.

In order to find the concentration of the methanol present at any time in the system, a calibration for the quantitative analysis has been done prior to the experiments and following equation has been obtained (see details in Supporting Information file and Fig. S4):

$$Y = 298077 * X$$

where, X and Y correspond to the area under the GC spectrum and concentration of methanol in ppm, respectively.

The fractional amount of methanol present at any time has been expressed in terms of the ratio C/C_0, where, C corresponds to a concentration at a given time, while C_0 is the initial concentration.

3. Results and discussion

3.1. Material characterization

3.1.1. Catalyst systems

All the as-synthesized catalysts have been characterized before electrospraying over electrospun membranes. The BET surface area of P25 increases from 52 m^2/g to 83 m^2/g, when milled for 2 h whereas it decreases to 73 m^2/g under prolonged 8 h milling (Table 1). Additionally, the pore size distribution shows a progressive shift towards lower pore diameters, from 450 Å for P25 to 150 Å for P25–2 h and 80 for P25–8 h (Fig. 2).

The powder-XRD has been employed to characterize structural modifications taking place at the pristine TiO_2 upon milling (Fig. 3).

For P25, the respective peaks have been indexed at 2Θ values of 25.3, 37.8, 48.1, 55.1, 62.7, 70.3, 75.1, 82.8 which correspond to the crystal planes (101), (103), (112), (200), (211), (204), (220), (215), (224) of the anatase phase (JCPDS File No. 96–900–9087). Similarly, on comparing the following 2Θ peaks at 27.4, 36.1, 41.3, 44.0, 54.1, 56.6, 64.0, 68.9 with the reference (JCPDS File No. 96–900–7433), the equivalent planes (110), (101), (111), (210), (211), (220), (310), (301) of rutile phase have been observed. The milling induces a progressive decrease of the anatase phase (from 88% of P25 to 53% of P25–2 h and 43% of P25–8 h) and an increase in the amount of high pressure/orthorhombic polymorphs from 32% (P25–2 h) to 57% (P25–8 h).

Table 1
General Characteristics of the Catalysts.

Catalyst	Surface Area	Polymorph Composition (%)[a]		
		Anatase	Rutile	High Pressure/Orthorhombic
P25	52	88	12	/
P25–2 h	83	53	15	32
P25–8 h	73	43	/	57

[a]: obtained by Rietveld refining method.

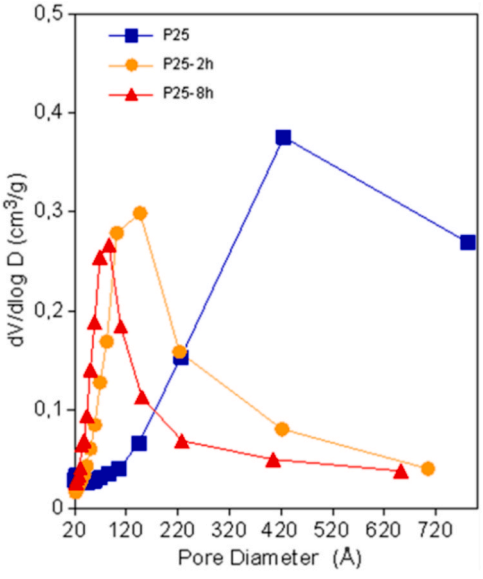

Fig. 2. Pore size distribution of the catalysts.

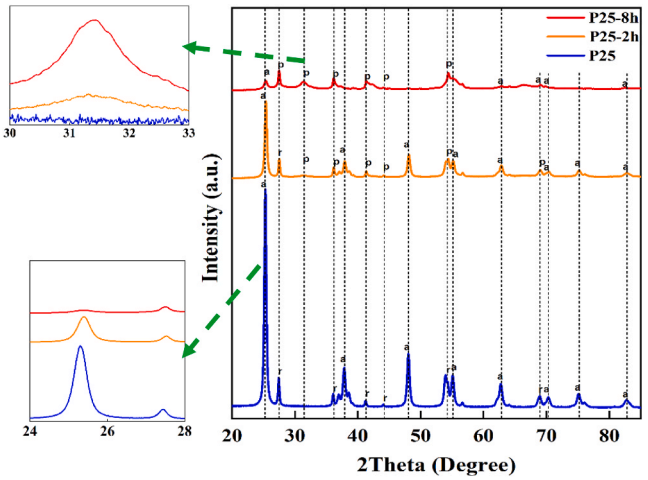

Fig. 3. Comparative XRD Diffraction patterns of the catalysts, a (=anatase), r (=rutile) and p (=high pressure/orthorhombic) polymorphs.

The effect of milling time over the crystal structure of reference TiO_2 is evident for the formation of additional crystal planes already in the case of P25–2 h. While the diffraction peaks at 25.4, 37.1, 37.9, 48.1, 55.1, 62.8, 70.3, 75.2, and 82.8 belong to the anatase, only two peaks belonging to the rutile phase have been observed at 27.5 and 56.6. The additional peaks with position 36.2, 41.4, 44.1, 54.5 and 68.9 belonging to the crystal planes (101), (111), (210), (211) and (301), correspond to another polymorph with tetragonal structure and has been reported to form at high pressure (JCPDS File No. 96–410–2356). Another peak at 31.3 (Fig. 3-inset), which was originally absent, has been observed with the crystal plane belonging to an orthorhombic polymorph of TiO_2, also forming under high pressure conditions (JCPDS File No. 96–231–2356). A similar trend has been observed in the case of P25–8 h, where the anatase phase fraction has been significantly reduced to 4 major peaks at 25.4, 48.1, 55.1 and 82.8, while no significant peak corresponded to the rutile phase were observed. However, the majority of peaks belonging to other polymorphs have become prominent with the replacement of the original phases. For comparison, the orthorhombic polymorph has appeared at positions 31.3, 42.2 and 66.6 with corresponding planes (111), (121) and (132), while the other polymorph 27.5, 36.2, 41.4, 54.4, 64.1 and 69.1 corresponds to the planes (110), (101), (111), (211), (310) and (301).

It has been reported that the formation of orthorhombic polymorph (TiO_2-II) is typical of high-pressure treatment of the commercial TiO_2, whereas further heat treatment of such high-pressure compound resulted in better photoactivity as compared to the pure material [18,19,29]. Such behavior, as the result of increased photocurrent, lowered charge recombination and enhanced light absorbance, can be attributed to the heterojunctions formed with anatase and rutile phases. Furthermore, an increased adsorption behavior has also been observed for material synthesized following the milling route.

The crystallinity for all three systems has been calculated and it follows an increasing trend from 92% for the pristine P25 to 94% and 97% for P25–2 h and P25–8 h samples respectively. The average crystallite size, calculated from Scherrer formula, follows a similar trend as it decreases from 19 nm for P25 to 14 nm and 9 nm for P25–2 h and P25–8 h respectively.

3.2. Catalytic membranes

The weight contents of catalyst nanoparticles for the three systems were calculated by the TGA analysis as shown in the Fig. 4(a), which displayed two distinct weight loss regions between 30 °C and 850 °C. The first step of weight loss, initiating at 150 °C, indicates the removal of water and remnant solvents adsorbed over the membrane surface. In the second step, the weight decreases continuously between 350 °C and 640 °C depicting the decomposition of polymeric content. With percentage of residual weights lying between 65% and 75%, the thermogram clearly indicates the consistency of electrospraying process. The FTIR spectra of catalytic membranes has been shown in.

Fig. 4(b). The characteristic peak of polyacrylonitrile at 2242 cm^{-1} corresponding to the -CN bond stretching while at 1452 cm^{-1} and 2938 cm^{-1} belonging to H-C-H bond bending and stretching, respectively, confirms the existence of polymeric background. The presence of the catalysts has not been evident in the FTIR analysis, which is because of their lower susceptibilities towards IR radiation and as a result of insignificant peaks in the spectra.

The quantitative measurements of the total catalytic content over membrane has been calculated using the final weight percentage from the thermogram and it has been summarized in Table 2. The initial area of the samples used in the TGA analyses were used to calculate the total and specific catalyst content.

The SEM and TEM images of all the catalytic systems are shown in Fig. 5. The increase of the milling time induces a less uniform deposition

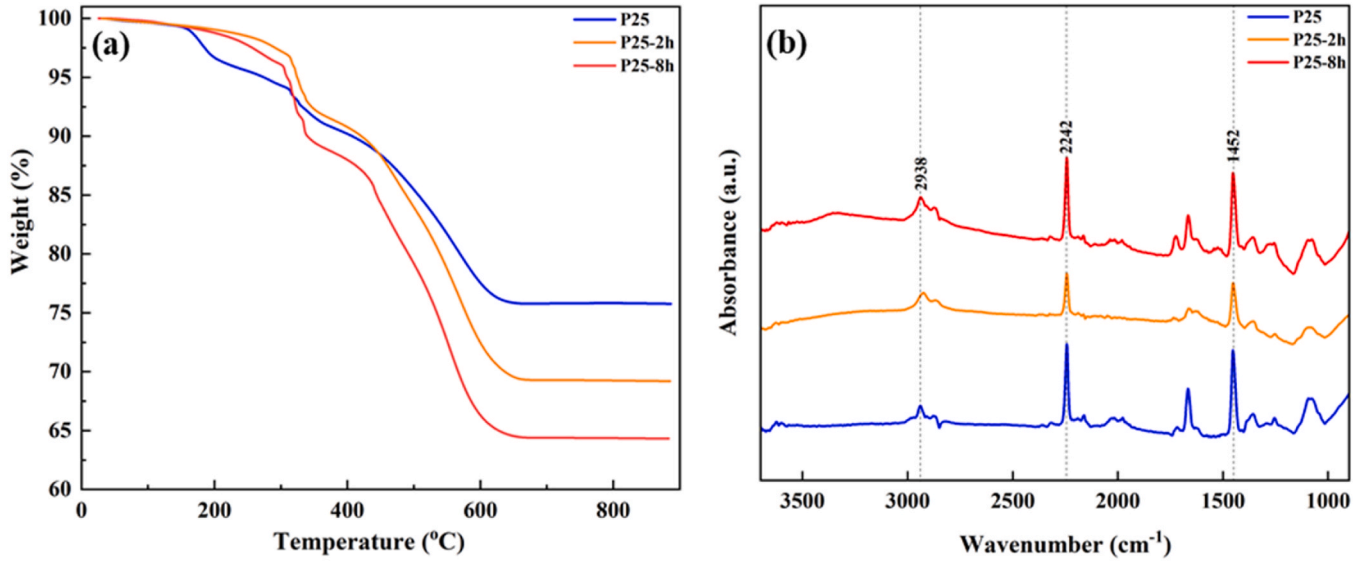

Fig. 4. (a) TGA thermograms, (b) Comparative IR spectra of catalyst coated membranes.

Table 2
Catalytic Composition of the Membranes.

Catalytic Mat	Photocatalyst content [mg]	Specific Catalyst Deposition [$x10^{-3}$ g/cm^2]
P25	264	0.98
P25–2 h	175	0.65
P25–8 h	169	0.63

of the catalyst on the membranes. The pristine P25 shows a highly uniform deposition most likely because of low possibility of aggregation whereas, in the milled samples, the aggregation behavior is more prominent. Such behavior can be attributed to the possible sintering of milled nanoparticles due to the high temperature and pressure that are commonly detected during the milling process. As clear from the TEM images (inset), the effect of milling process over the morphology is significant since the individual particle has become more spherical as compared to the pristine P25 where particle morphology is close to cubical.

3.3. Photocatalytic studies

All the experiments have been carried out in the batch mode under UV-irradiation. Blank experiment has also been performed prior to the experiments and there was no impact of UV-irradiation over the methanol concentration in the absence of catalyst. The VOC concentration used in this study includes high as well as low concentration ranges. Initially, all the three catalysts have been investigated for a high concentration range (2150 ppm).

As can be seen in Fig. 6, the P25–2 h system performs better than the pristine catalyst P25 (respectively 69% and 62% abatement). Interestingly, the P25–8 h sample exhibits a poor performance with only about 43% removal which illustrates the effect of milling time over efficiency.

In the following studies, with regard to the lower VOC concentration, the experiments have been carried out involving P25 and P25–2 h systems, given their promising activity.

in the preceding experiments. The concentration of methanol in the lower range (Fig. 7) has been maintained between 73 and 78 ppm, which is in good agreement with the permissible VOC limit in a closed environment, and thus is able to mimic the degradation pathway. In this case, the difference between the activity of the two catalytic systems has become sharper. Indeed, while, P25–2 h achieves almost a complete abatement, P25 only attains ~4% of removal (Fig. 7). Remarkably, in this case the complete degradation was possible within 40 min as compared to the experiments carried out with the higher concentration.

The conversion trend of methanol to methyl formate can be followed in Fig. 8. P25–2 h achieved the highest formation of product in agreement with the degradation plot of methanol (Fig. 6(a)). The low fraction of methyl formate in the case of P25–8 h is justified, given the lower photoactivity of the catalyst. In Fig. 8(b), the large difference in the methyl formate generation in the case of low initial pollutant concentration is also consistent with that of Fig. 7(a).

The quantification of by-products formed during the photocatalytic experiments was not possible, as the large variations during the repetitive runs led to lack of reliability of the data obtained.

The rates of reaction have been calculated and they follow the first (pseudo) order kinetics with rate constants for P25–2 h being the highest

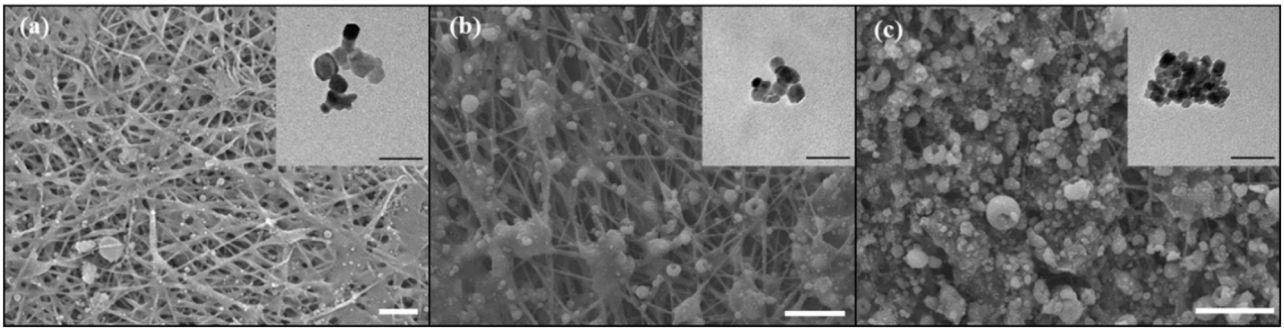

Fig. 5. SEM images of catalyst coated membranes (a) P25, (b) P25–2 h, (c) P25–8 h. (Scale – 10 μm) Corresponding TEM images of the nanoparticles has been shown in the inset (scale – 50 nm).

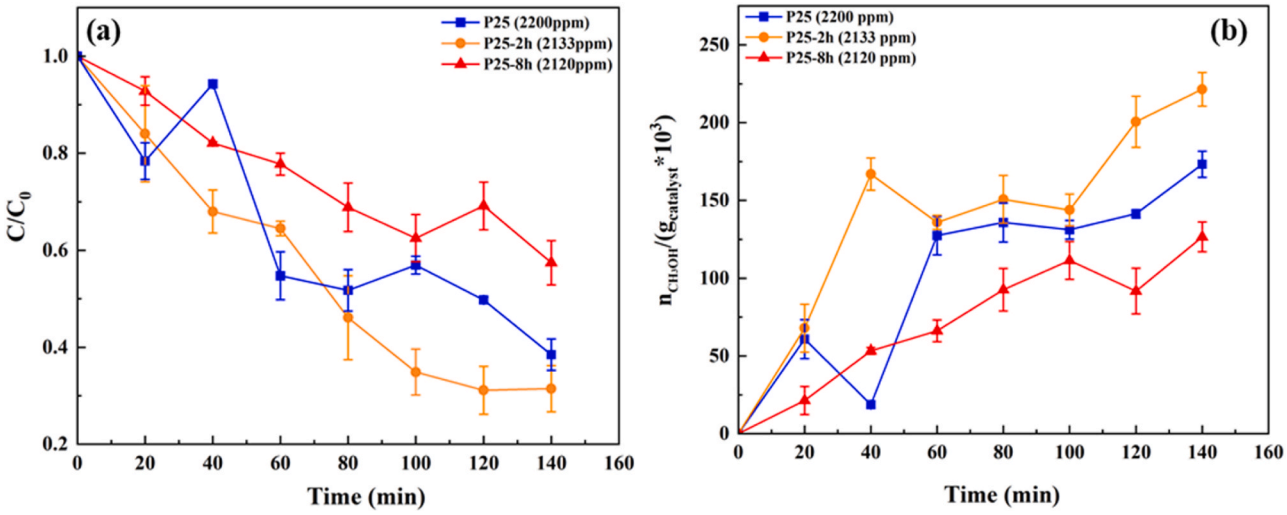

Fig. 6. (a) Degradation behavior for High Methanol concentration, (b) No. of moles reacted per gram of catalysts.

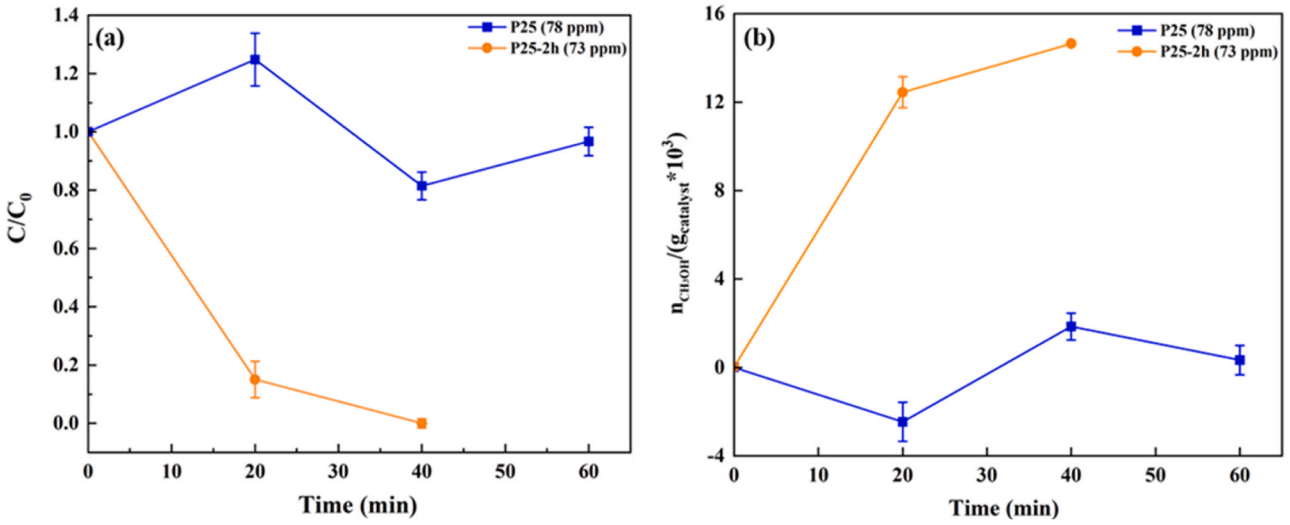

Fig. 7. (a) Degradation behavior for High Methanol concentration, (b) No. of moles reacted per gram of catalysts.

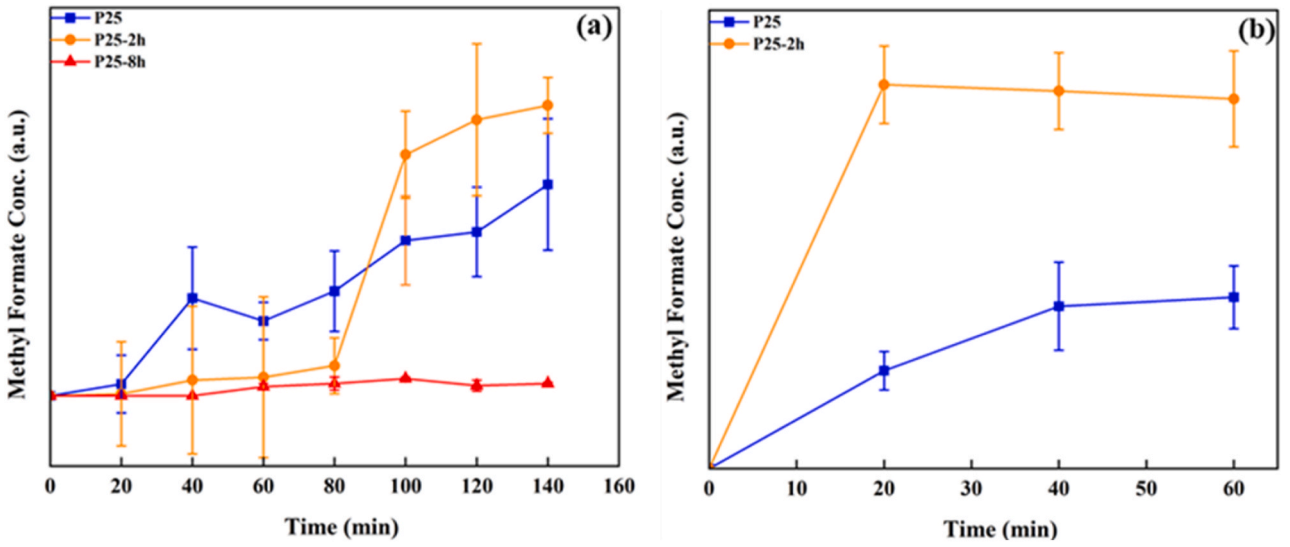

Fig. 8. Methyl formate generation trends for (a) High and, (b) Low Methanol Concentrations.

among the three (Table 3). Furthermore, the R-square values corresponding to high and low methanol concentrations for P25–2 h are reasonable. Whereas, in the case of P25 the poor R-square value for a low methanol concentration can be argued upon the fact that the removal efficiency was the insignificant (~4%) and due to the adsorption-desorption behavior of P25 towards methanol [35,36]. Hence, because of indistinguishability between the extent of adsorption and degradation of methanol over P25, it was not possible to obtain a reliable fitting and thus the actual rate of reaction.

The plots of -ln(C/C0) vs. time for all the system follow the linear equations as shown in Fig. 9. Since the slope of this plot is inferred as the rate constant, P25–2 h shows the higher rate of reaction compared to the other samples. In addition, a substantial difference between the rates can be found when investigating high or low concentration of pollutant. Such a high rate can be associated with increased formation of charge carriers [30].

Furthermore, the high pressure TiO_2-II phase has shown a downward shift in the fermi-level which also contributes towards the photoactivity of the current catalyst [30]. The pristine TiO_2, which is significantly active under the UV-radiation has been reported to show visible light activity after a high-pressure treatment followed by annealing [31]. The higher activity of P25–2 h can be related to the formation of high pressure TiO_2-II phase during the milling process, while under prolonged milling time, sintering of the particles and the decrease of the surface area induce further reduction of the activity. The poor performance of P25–8 h system can be explained on the behalf of the effect of milling time over photoactivity.

It has been previously reported that the activity of TiO_2 decreases with an increase in milling time [32–34].

When exposed to a methanol environment, the TiO_2 surface has been reported to adsorb the organic compound and adsorption phenomena is

Table 3
Kinetics of the Catalytic Membranes.

Catalytic Mat	Avg. Rate Constant (x10^{-3} min^{-1})	R-square (COD)	Std. Dev.	Methanol Concentration (High/Low)
P25	6.17	0.88	0.00092	High
	11.22	0.54	0.00059	Low
P25–2 h	9.37	0.95	0.00085	High
	339	0.92	0.09779	Low
P25–8 h	4.28	0.94	0.00043	High

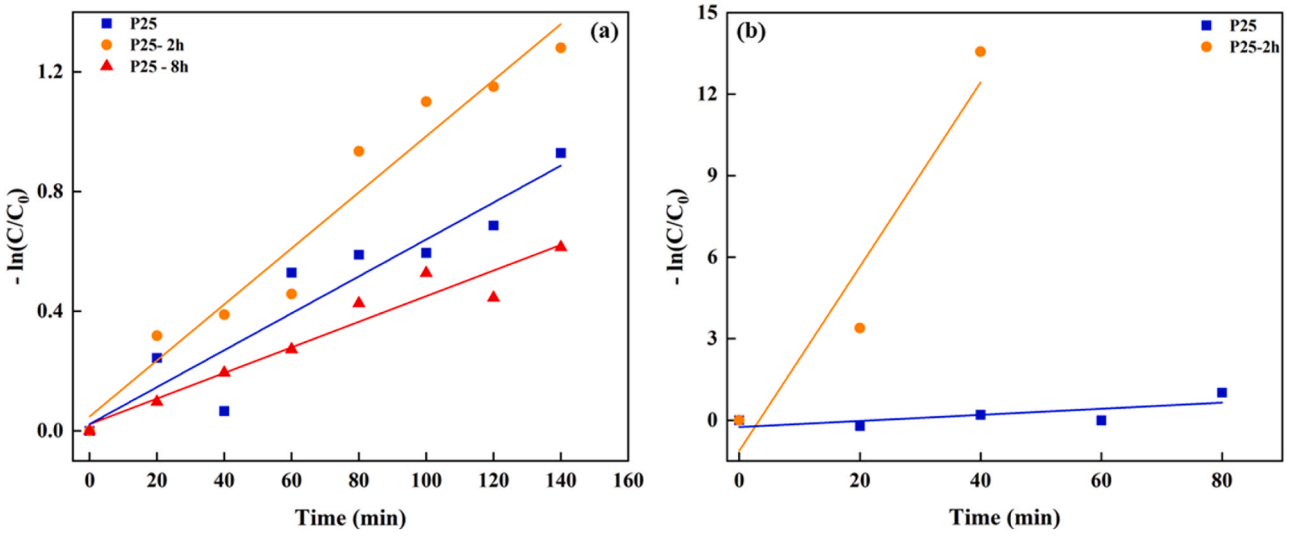

Fig. 9. Pseudo first order kinetics for (a) High and, (b) Low Methanol Concentrations.

proposed to follow dissociative as well as non-dissociative pathways [35,36]. The dissociative adsorption results in the formation of methoxy groups and associated protons, which are stable at the room temperature, attached to the defect sites present on the catalyst surface, and thus, it's possible to increase the adsorption of methoxy groups by increasing the number of surface defects [35]. The Ti^{4+}_{5c} (c = coordination number) surface sites serve as the favorable binding locations for methoxy groups after dissociative adsorption, the adsorbed methoxy groups then act as the hole traps during UV-irradiation. Moreover, the Ti sites adjacent to the methoxy-bound sites also assist in the entrapment of electrons emitted during the conversion of methoxy groups to formate [37].

The reaction towards adsorption of methoxy groups from methanol follows the following pathways:

$$Ti^{4+}_{5c} + CH_3OH + O^{2-}_{br} \rightarrow Ti^{4+}_{5c}\ O^{-}CH_3 + HO^{-}_{br} \quad (3)$$

$$2Ti^{4+}_{5c} + CH_3OH + O^{2-}_{br} \rightarrow (Ti^{4+}_{5c})_2\ O^{-}CH_3 + HO^{-}_{br} \quad (4)$$

Here, the proton is extracted from the hydroxyl group present in methanol facilitated by the bridging oxygen anion (O^{2-}_{br}), which is the oxygen vacancy between two Ti^{3+} sites. It has been proposed that these bridging oxygen anions form band gap states about 1 eV below the conduction band minimum [38]. The generated methoxy group seems to be coordinatively bonded with unsaturated Ti cation (Ti^{4+}_{5c}) in single (1) or bridged configuration (2) and is highly stable at room temperature [39–42].

These species, then, act towards the trapping of photo-generated holes further promoting the formate production which can be explained as the lowered position of highest occupied molecular orbitals of the surface bound methoxy groups with respect to valence-band maximum of TiO_2, which makes the adsorbed methoxy groups as the preferable hosts for the holes as compared to methanol [42]. The charge carrier separation plays a vital role for the overall efficiency of photocatalysis, and it is important to highlight the parameters influencing the trapping of holes as well as the electrons generated during the irradiation. It has been suggested that under aerobic conditions, the oxygen present in the reaction environment acts as an electron scavenger apart from taking part in the succeeding reactions [43,44]. The scavenging of electrons enhances oxidation rate and thus the reaction shifts towards product side i.e. formates. which otherwise would have led to blocking of acceptor sites by charge (e^-) accumulation. Han et al. explored the oxidation pathways of methanol to methyl formate and found out that the charge carrier separation by electron scavenging plays a trivial role in the formation of methyl formate apart from the importance of surface adsorbed methoxy groups [45].

Different mechanisms of formation of methyl formate from methanol have been postulated in previous studies. For example, Yu et al. in their studies observed the direct oxidation of methanol to methyl formate which was associated with the interaction of adsorbed formate species with surrounding methanol molecules [46].

There is also the possibility of conversion of methoxy groups into formaldehyde by the elimination of β-H which also remain adsorbed on the surface, as reported by Whiting et al. But the presence of formaldehyde in the recirculated stream is not evident in the current studies, since the report also suggests that the formaldehyde molecules remain adsorb to the active sites at ambient temperature and further take part in coupling reaction with the neighboring adsorbed methoxy groups to form methyl formate [47].

Such a pathway, involving surface adsorbed formaldehyde as an intermediate, during the photo-oxidation of CH_3OH on the TiO_2 surface, follows the mechanism as described by Wang et al. [48].

$$Ti^{4+}_{5c} + CH_3OH + O^{2-}_{br} \rightarrow Ti^{4+}_{5c} - O^{-}CH_{3(ads)} + HO^{-}_{br}$$

$$Ti^{4+}_{5c} - O^{-}CH_{3(ads)} + O^{2-}_{br} \longrightarrow^{hv} HCHO_{(ads)} + HO^{-}_{br}$$

$$HCHO_{(ads)} + O^{2-}_{br} \longrightarrow^{hv} HCHO_{(ads)} + HO^{-}_{br}$$

$$CH_3O_{(ads)} + HCO_{(ads)} \longrightarrow^{hv} HCOOCH_{3(ads)}$$

In the proposed mechanism, the role of surface adsorbed species is comprehensible attributed to their photocatalytic reactivity as a result of adsorption of catalyst surface [48]. The conversion of methanol in the current work is supposed to follow aforementioned mechanism, which further coincides with our previous findings [10].

A summary of relevant study carried out by researchers has been listed in Table 4. The investigations often employ several chemical precursors to obtain the catalyst with desired properties [50–53]. Moreover, they also include secondary nanostructures to enhance the performance which further make the process cumbersome [49,51,52,61], require high pressure-temperature conditions [50,53,54] and post-treatment [54,57].

In the study presented here, a novel approach towards the fabrication of photoactive media based on nanostructures have been proposed. The current work, when compared with previous research with similar classes of catalyst/pollutant, provides an alternative pathway with a simplified overall process, while, simultaneously lowers the overall chemical requirements during the process and thus lowering the (direct

Table 4
A Comparative Analysis of Earlier Relevant Studies.

Year	Catalyst	Fabrication Method/ Process	Target VOC	Concentration	Removal Efficiency (%)	Irradiation Time (min)	Irradiation Source
2018	CQDs/TiO_2	Hydrothermal	Acetaldehyde	500 ppm	99	120	UV [49]
2018	rGO/ TiO_2	Hydrothermal	Formaldehyde	200 ppm	88.3	240	Vis [50]
2017	TiO_2 NF/ACF	Hydrothermal	Toluene	230 ppm	100	120	UV [51]
2020	CeO_2/TiO_2/ACF	Sol-gel	Toluene	92.8 ppm	90	360	UV [52]
2018	CDs/CdS-TiO_2	Hydrothermal-precipitation-calcination	Benzene	30 ppm	93.8	60	Vis [53]
2020	TiO_2/diatomite	Hydrolysis precipitation and calcination crystallization	Acetone, MEK	10 ppm	~42–61	~40	UV [54]
2018	TiO_2	Commercial	Ethanol	0.2–2 ppm	~4–44	—	UV [55]
2022	Pt-TiO_2	Wet-impregnation	Iso-butanol	<1 ppm	100	150	UV [56]
2010	TiO_2 thin film	Sol-gel	Acetone, toluene, p-xylene	0.1–0.3 mol/m^3	~55–77	480	UV [57]
2012	TiO_2	Commercial	Benzene+Methanol	0.9μmol L^{-1}	55–80	90	UV [58]
2009	TiO_2	Thermohydrolysis	Methanol, n-octane	~60–200ppmv	~90–99	300	UV [59]
2010	TiO_2	Commercial	Methanol	-	-	300	UV [60]
2008	SiO_2-TiO_2 composite pellets	Sol-gel	Methanol	50ppmv	-	1500	UV [61]
2005	WO_3-TiO_2	Mechanosynthesis	monocrotophos	10−4 mol/L	38.3	10	UV [62]
2023	C-N/TiO_2	Mechanosynthesis	Nitric oxide	500 ± 50ppbv	48	105	Vis [63]
2016	CNT/TiO_2	Electrospinning+Thermal Treatment	Benzene	100 ppm	52	90	Vis [64]
2017	TiO_2	Electrospinning+Electrospraying (Simultaneous)	Toluene	325 ± 50mgm^{-3}	78.6	120	Xenon [65]
2021	TiO_2	Emulsion Electrospinning	NO gas	1ppmv (continuous mode)	78.6	60	UV [66]
2017	rGO/TiO_2	Emulsion Electrospinning	Methanol	4000 ± 200 ppm	100	300	UV [67]
2020	GO/TiO_2	Solvothermal+Electrospinning	Methanol	530 ± 40 ppm	100	40	UV [68]
This work	**TiO_2**	**Mechano-synthesis+Electrospraying + Electrospinning**	**Methanol**	**75 & 2150 ppm**	**100 & 69**	**40 & 140**	**UV**

or indirect) energy consumption. (Table 4).

4. Conclusion

In the current work, the effects of mechanosynthesis over catalytic activity of TiO_2-based materials towards gas-phase photodegradation of methanol has been investigated. It has been observed that the milling time has a significant impact over the photoactivity of TiO_2 systems. Although there is an increase in the activity which has been attributed to the formation of photoactive TiO_2-II crystal phase, it is observed that further increasing the milling time can lead to inactivity of an originally active catalyst. The drastic change in catalytic behavior has been ascribed to the lattice distortion of the crystal structure as well as agglomeration of nanoparticles which screen the number of active sites present on the catalyst surface.

Here, a facile and solvent free route of increasing the activity of commercial TiO_2 has been investigated by optimizing the process time of the mechanosynthesis route, and application of the as-treated catalyst immobilized over nanofibrous polymer matrix, towards abatement of methanol has been carried out. The TiO_2 sample milled for 2 h has demonstrated promising activity towards VOC degradation at significantly lower concentration closely mimicking the actual levels in a closed environment. While, a rational comparison made in Table 4 with the previous studies, further elucidates the applicability of methodology proposed in this work, thanks to the simplified processes which are both time and energy efficient and hence resulting in a cost-effective product with superior performance. To the best of our knowledge, the current study is first of its kind and offers a sustainable path towards the mitigation indoor air pollutants.

CRediT authorship contribution statement

Martina Roso Conceptualization, Methodology, Supervision, Validation, Project administration, Funding acquisition, Writing - Review & Editing. **Abhishek Anand** Writing - Original Draft, Investigation, Visualization, Software. **Eleonora Aneggi** Investigation, Validation, Writing - Review & Editing **Carlo Boaretti**, **Alessandra Lorenzetti, Alessandro Trovarelli** and **Michele Modesti** Validation, Visualization, Writing - Review & Editing.

Declaration of Competing Interest

The authors declare that they have no known competing financial interests or personal relationships that could have appeared to influence the work reported in this paper.

Data Availability

Data will be made available on request.

Acknowledgment

The project was funded in the framework of the program "BIRD 2020″ promoted by University of Padova (project code ROSO_BIRD2020_01).

Appendix A. Supporting information

Supplementary data associated with this article can be found in the online version at doi:10.1016/j.jece.2023.111595.

References

[1] Hangjuan Ren, Pramod Koshy, Wen-Fan Chen, Shaohua Qi, Charles Christopher Sorrell, Photocatalytic materials and technologies for air purification, J. Hazard. Mater. 325 (2017) 340–366.

[2] Mamaghani, Alireza Haghighat, Fariborz Haghighat, Chang-Seo Lee, Photocatalytic oxidation technology for indoor environment air purification: the state-of-the-art, Appl. Catal. B: Environ. 203 (2017) 247–269.

[3] Zijian Dai, Jie Zhu, Jiaqi Yan, Jiafei Su, Yunfei Gao, Xing Zhang, Qinfei Ke, Gregory N. Parsons, An advanced dual-function MnO_2-fabric air filter combining catalytic oxidation of formaldehyde and high-efficiency fine particulate matter removal, Adv. Funct. Mater. 30 (42) (2020), 2001488.

[4] Shenghao Zhao, Yang Yang, Fukun Bi, Yifan Chen, Minghong Wu, Xiaodong Zhang, Guan Wang, Oxygen vacancies in the catalyst: Efficient degradation of gaseous pollutants, Chem. Eng. J. 454 (2023), 140376.

[5] Jonas Baltrusaitis, Jennifer Schuttlefield, Elizabeth Zeitler, Vicki H. Grassian, Carbon dioxide adsorption on oxide nanoparticle surfaces, Chem. Eng. J. 170 (2–3) (2011) 471–481.

[6] Subramanian Sundarrajan, Kwong Luck Tan, Soon Huat Lim, Seeram Ramakrishna, Electrospun nanofibers for air filtration applications, Procedia Eng. 75 (2014) 159–163.

[7] Lale I.ş.ıkel Şanlı, Begüm Yarar, Vildan Bayram, Selmiye Alkan Gürsel, Electrosprayed catalyst layers based on graphene–carbon black hybrids for the next-generation fuel cell electrodes, J. Mater. Sci. 52 (2017) 2091–2102.

[8] Carlo Boaretti, Martina Roso, Michele Modesti, Alessandra Lorenzetti, Ultrasound-promoted abatement of formaldehyde in liquid phase with electrospun nanostructured membranes: the synergy of combined AOPs, Nanomaterials 13 (3) (2023) 435.

[9] Yanan Liu, He Lv, Yang Liu, Yiman Gao, Hak Yong Kim, Yuanming Ouyang, Deng-Guang Yu, Progresses on electrospun metal–organic frameworks nanofibers and their wastewater treatment applications, Mater. Today Chem. 25 (2022), 100974.

[10] Martina Roso, Carlo Boaretti, Maria Guglielmina Pelizzo, Annamaria Lauria, Michele Modesti, Alessandra Lorenzetti, Nanostructured photocatalysts based on different oxidized graphenes for VOCs removal, Ind. Eng. Chem. Res. 56 (36) (2017) 9980–9992.

[11] Martina Roso, Carlo Boaretti, Renato Bonora, Michele Modesti, Alessandra Lorenzetti, Nanostructured active media for volatile organic compounds abatement: The synergy of graphene oxide and semiconductor coupling, Ind. Eng. Chem. Res. 57 (49) (2018) 16635–16644.

[12] Tan Xing, Jaka Sunarso, Wenrong Yang, Yongbai Yin, Alexey M. Glushenkov, Lu. Hua Li, Patrick C. Howlett, Ying Chen, Ball milling: a green mechanochemical approach for synthesis of nitrogen doped carbon nanoparticles, Nanoscale 5 (17) (2013) 7970–7976.

[13] Achim Stolle, Brindaban Ranu, Ball Milling Towards Green Synthesis: Applications, Projects, Challenges, Royal Society of Chemistry, 2014.

[14] Eleonora Aneggi, Veronica Rico-Perez, Carla de Leitenburg, Stefano Maschio, Lluís Soler, Jordi Llorca, Alessandro Trovarelli, Ceria–zirconia particles wrapped in a 2D carbon envelope: improved low-temperature oxygen transfer and oxidation activity, Angew. Chem. Int. Ed. 54 (47) (2015) 14040–14043.

[15] Eleonora Aneggi, Jordi Llorca, Alessandro Trovarelli, Mimoun Aouine, Philippe Vernoux, In situ environmental HRTEM discloses low temperature carbon soot oxidation by ceria–zirconia at the nanoscale, Chem. Commun. 55 (27) (2019) 3876–3878.

[16] Sander Ratso, Moulay Tahar Sougrati, Maike Kääärik, Maido Merisalu, Mihkel Rähn, Vambola Kisand, Arvo Kikas, et al., Effect of ball-milling on the oxygen reduction reaction activity of iron and nitrogen co-doped carbide-derived carbon catalysts in acid media, ACS Appl. Energy Mater. 2 (11) (2019) 7952–7962.

[17] Jing He, Peiwen Wu, Linjie Lu, Hongping Li, Haiyan Ji, Minqiang He, Qingdong Jia, Mingqing Hua, Wenshuai Zhu, Huaming Li, Lattice-refined transition-metal oxides via ball milling for boosted catalytic oxidation performance, ACS Appl. Mater. Interfaces 11 (40) (2019) 36666–36675.

[18] Suchitra Sen, Moti Lal Ram, S. Roy, Bijit Kumar Sarkar, The structural transformation of anatase TiO2 by high-energy vibrational ball milling, J. Mater. Res. 14 (3) (1999) 841–848.

[19] Matías Gastón Rinaudo, Ana M. Beltrán, María Asunción Fernández, Luis Eduardo Cadús, Maria Roxana Morales, Tailoring materials by high-energy ball milling: TiO2 mixtures for catalyst support application, Mater. Today Chem. 17 (2020), 100340.

[20] Suryanarayana, C. Mechanical Alloying and Milling Marcel Dekker. Ee. Uu (2004): 59–78.

[21] David M. Lunderberg, K.Misztal Pawel, Yingjun Liu, Caleb Arata, Yilin Tian, Kasper Kristensen, Robert J. Weber, William W. Nazaroff, Allen H. Goldstein, High-resolution exposure assessment for volatile organic compounds in two California residences, Environ. Sci. Technol. 55 (10) (2021) 6740–6751.

[22] Yingjun Liu, Pawel K. Misztal, Jianyin Xiong, Yilin Tian, Caleb Arata, Robert J. Weber, William W. Nazaroff, Allen H. Goldstein, Characterizing sources and emissions of volatile organic compounds in a northern California residence using space-and time-resolved measurements, Indoor Air 29(4) (2019) 630–644.

[23] Xiaochen Tang, K.Misztal Pawel, William W. Nazaroff, Allen H. Goldstein, Volatile organic compound emissions from humans indoors, Environ. Sci. Technol. 50 (23) (2016) 12686–12694.

[24] S.J. Solomon, G.W. Schade, J. Kuttippurath, A. Ladstätter-Weissenmayer, J. P. Burrows, VOC concentrations in an indoor workplace environment of a university building, Indoor Built Environ. 17 (3) (2008) 260–268.

[25] Millet, D.B. Daniel, J. Jacob, T.G. Custer, J.A. De Gouw, A.H. Goldstein, T. Karl, H. B. Singh, et al., New constraints on terrestrial and oceanic sources of atmospheric methanol, Atmos. Chem. Phys. 8 (23) (2008) 6887–6905.

[26] Robert Alan Young, The rietveld method, Int. Union Crystallogr. Vol. 5 (1993).

[27] Brian H. Toby, EXPGUI, a graphical user interface for GSAS, J. Appl. Crystallogr. 34 (2) (2001) 210–213.

[28] Larson, A.C., R.B. Von Dreele. General Structure Analysis System (GSAS), Los Alamos National Lab Report (LAUR) 86–748. Search in (2000).

[29] Saeid Akrami, Monotori Watanabe, Tan Hui Ling, Tatsumi Ishihara, Makoto Arita, Masayoshi Fuji, Kaveh Edalati, High-pressure TiO_2-II polymorph as an active photocatalyst for CO_2 to CO conversion, Appl. Catal. B: Environ. 298 (2021), 120566.

[30] Kaveh Edalati, Qing Wang, Hiroto Eguchi, Hadi Razavi-Khosroshahi, Hoda Emami, Miho Yamauchi, Masayoshi Fuji, Zenji Horita, Impact of TiO_2-II phase stabilized in anatase matrix by high-pressure torsion on electrocatalytic hydrogen production, Mater. Res. Lett. 7 (8) (2019) 334–339.

[31] Qing Wang, Motonori Watanabe, Kaveh Edalati, Visible-light photocurrent in nanostructured high-pressure TiO2-II (columbite) phase, J. Phys. Chem. C. 124 (25) (2020) 13930–13935.

[32] Theivasanthi, T. Review on Titania Nanopowder-Processing and Applications. arXiv preprint arXiv:1704.00981 (2017).

[33] Mei Wang, Qianfei Zhao, He Yang, Dai Shi, Juncen Qian, Photocatalytic antibacterial properties of copper doped TiO2 prepared by high-energy ball milling, Ceram. Int. 46 (10) (2020) 16716–16724.

[34] Marica Muscetta, Samar Al Jitan, Giovanni Palmisano, Roberto Andreozzi, Raffaele Marotta, Stefano Cimino, Ilaria Di Somma, Visible light–driven photocatalytic hydrogen production using Cu2O/TiO2 composites prepared by facile mechanochemical synthesis, J. Environ. Chem. Eng. 10 (3) (2022), 107735.

[35] Li-Qiong Wang, F.Ferris Kim, J.P. Winokur, Ashley N. Shultz, Donald R. Baer, Mark H. Engelhard, Interactions of methanol with stoichiometric and defective TiO_2 (110) and (100) surfaces, J. Vac. Sci. Technol. A: Vac. Surf. Films 16 (5) (1998) 3034–3040.

[36] Enrique Farfan-Arribas, J.ürgen Biener, Cynthia M. Friend, Robert J. Madix, Reactivity of methanol on TiO_2 nanoparticles supported on the Au (111) surface, Surf. Sci. 591 (1–3) (2005) 1–12.

[37] Dimitar A. Panayotov, Steven P. Burrows, John R. Morris, Photooxidation mechanism of methanol on rutile TiO_2 nanoparticles, J. Phys. Chem. C 116 (11) (2012) 6623–6635.

[38] Michael A. Henderson, A surface science perspective on TiO_2 photocatalysis, Surf. Sci. Rep. 66 (6–7) (2011) 185–297.

[39] Dimitar A. Panayotov, Steven Burrows, Mihail Mihaylov, Konstantin Hadjiivanov, Brian M. Tissue, John R. Morris, Effect of methanol on the Lewis acidity of rutile TiO_2 nanoparticles probed through vibrational spectroscopy of coadsorbed CO, Langmuir 26 (11) (2010) 8106–8112.

[40] Enrique Farfan-Arribas, Robert J. Madix, Different binding sites for methanol dehydrogenation and deoxygenation on stoichiometric and defective TiO_2 (110) surfaces, Surf. Sci. 544 (2–3) (2003) 241–260.

[41] Antonio Tilocca, Annabella Selloni, Methanol adsorption and reactivity on clean and hydroxylated anatase (101) surfaces, J. Phys. Chem. B 108 (50) (2004) 19314–19319.

[42] Jin Zhao, Jinlong Yang, Hrvoje Petek, Theoretical study of the molecular and electronic structure of methanol on a TiO_2 (110) surface, Phys. Rev. B 80 (23) (2009), 235416.

[43] William Balcerski, Su. Young Ryu, Michael R. Hoffmann, Gas-phase photodegradation of decane and methanol on: dynamic surface chemistry characterized by diffuse reflectance FTIR, Int. J. Photo 2008 (2008).

[44] Chih-Chung Chuang, Chih-Cheng Chen, Jong-Liang Lin, Photochemistry of methanol and methoxy groups adsorbed on powdered TiO_2, J. Phys. Chem. B 103 (13) (1999) 2439–2444.

[45] Chenhui Han, Xuzhuang Yang, Guanjun Gao, Jie Wang, Huailiang Lu, Jie Liu, Min Tong, Xiaoyuan Liang, Selective oxidation of methanol to methyl formate on catalysts of Au–Ag alloy nanoparticles supported on titania under UV irradiation, Green. Chem. 16 (7) (2014) 3603–3615.

[46] K.M.Kerry Yu, Connie M.Y. Yeung, Shik Chi Tsang, Carbon dioxide fixation into chemicals (methyl formate) at high yields by surface coupling over a Pd/Cu/ZnO nanocatalyst, J. Am. Chem. Soc. 129 (20) (2007) 6360–6361.

[47] Gareth T. Whiting, Simon A. Kondrat, Ceri Hammond, Nikolaos Dimitratos, Qian He, David J. Morgan, Nicholas F. Dummer, et al., Methyl formate formation from methanol oxidation using supported gold–palladium nanoparticles, ACS Catal. 5 (2) (2015) 637–644.

[48] Zhengming Wang, Qing Yuan, Zhen Zhang, Feng Xiong, Guanghui Sun, Hong Xu, Peng Chai, Weixin Huang, On the mechanism of methyl formate production initiated by photooxidation of methanol on rutile TiO_2 (110) and TiO_2 (011)-(2×1) surfaces, J. Phys. Chem. C 123 (51) (2019) 31073–31081.

[49] Yidan Hu, Xiaofeng Xie, Xiao Wang, Yan Wang, Yi Zeng, David Y.H. Pui, Jing Sun, Visible-light upconversion carbon quantum dots decorated TiO2 for the photodegradation of flowing gaseous acetaldehyde, Appl. Surf. Sci. 440 (2018) 266–274.

[50] Lian Yu, Long Wang, Xibo Sun, Daiqi Ye, Enhanced photocatalytic activity of rGO/TiO2 for the decomposition of formaldehyde under visible light irradiation, J. Environ. Sci. 73 (2018) 138–146.

[51] Ming-Jun Tian, Fang Liao, Qin-Fei Ke, Ya-Jun Guo, Ya-Ping Guo, Synergetic effect of titanium dioxide ultralong nanofibers and activated carbon fibers on adsorption and photodegradation of toluene, Chem. Eng. J. 328 (2017) 962–976.

[52] Qiyuan Chen, Lu Liu, Lifen Liu, Yizhen Zhang, A novel UV-assisted PEC-MFC system with CeO2/TiO2/ACF catalytic cathode for gas phase VOCs treatment, Chemosphere 255 (2020), 126930.

[53] Meng Wang, Jianhao Hua, Yaling Yang, Fabrication of CDs/CdS-TiO2 ternary nano-composites for photocatalytic degradation of benzene and toluene under visible light irradiation, Spectrochim. Acta Part A: Mol. Biomol. Spectrosc. 199 (2018) 102–109.

[54] Guangxin Zhang, Arman Peyravi, Zaher Hashisho, Zhiming Sun, Yangyu Liu, Shuilin Zheng, Lexuan Zhong, Integrated adsorption and photocatalytic degradation of VOCs using a TiO 2/diatomite composite: effects of relative humidity and reaction atmosphere, Catal. Sci. Technol. 10 (8) (2020) 2378–2388.
[55] Lexuan Zhong, Fariborz Haghighat, Modeling of by-products from photocatalytic oxidation (PCO) indoor air purifiers: a case study of ethanol, Build. Environ. 144 (2018) 427–436.
[56] Ji-Won You, Kumar Vikrant, Dae-Hwan Lim, Swati Verma, Deepak Kukkar, Hassan Anwer, Ki-Hyun Kim, Photocatalytic potential of a titanium dioxide–supported platinum catalyst against VOCs with complicated composition under varying humidity conditions, J. Clean. Prod. 371 (2022), 133487.
[57] Wen J. Liang, Jian Li, Yu.Q. Jin, Photocatalytic degradation of gaseous acetone, toluene, and p-xylene using a TiO2 thin film, J. Environ. Sci. Health Part A 45 (11) (2010) 1384–1390.
[58] Geng Qijin, Wang Qingming, Zhang Bin, Adsorption and photocatalytic oxidation of methanol–benzene binary mixture in an annular fluidized bed photocatalytic reactor, Ind. Eng. Chem. Res. 51 (47) (2012) 15360–15373.
[59] J.érôme Taranto, Didier Frochot, Pierre Pichat, Photocatalytic treatment of air: comparison of various TiO2, coating methods, and supports using methanol or n-octane as test pollutant, Ind. Eng. Chem. Res. 48 (13) (2009) 6229–6236.
[60] Hiroshi Kominami, Hiroshi Sugahara, Keiji Hashimoto, Photocatalytic selective oxidation of methanol to methyl formate in gas phase over titanium (IV) oxide in a flow-type reactor, Catal. Commun. 11 (5) (2010) 426–429.
[61] Jennifer M. Stokke, W.Mazyck David, Photocatalytic degradation of methanol using silica–titania composite pellets: effect of pore size on mass transfer and reaction kinetics, Environ. Sci. Technol. 42 (10) (2008) 3808–3813.
[62] Chen Shifu, Chen Lei, Gao Shen, Cao Gengyu, The preparation of coupled WO3/TiO2 photocatalyst by ball milling, Powder Technol. 160 (3) (2005) 198–202.
[63] Alessia Zollo, Stefano Livraghi, Elio Giamello, Andrea Cioni, Valentina Dami, Giada Lorenzi, Giovanni Baldi, CN co-doped titanium dioxide. Key aspects in the assessment of the air pollutants abatement capability, J. Environ. Chem. Eng. 11 (2) (2023), 109451.
[64] Mathana Wongaree, Siriluk Chiarakorn, Surawut Chuangchote, Takashi Sagawa, Photocatalytic performance of electrospun CNT/TiO 2 nanofibers in a simulated air purifier under visible light irradiation, Environ. Sci. Pollut. Res. 23 (2016) 21395–21406.
[65] Jiafei Su, Guohong Yang, Cuilian Cheng, Chen Huang, He Xu, Qinfei Ke, Hierarchically structured TiO2/PAN nanofibrous membranes for high-efficiency air filtration and toluene degradation, J. Colloid Interface Sci. 507 (2017) 386–396.
[66] Miyeon Kwon, Juhea Kim, Juran Kim, Photocatalytic activity and filtration performance of hybrid TiO2-cellulose acetate nanofibers for air filter applications, Polymers 13 (8) (2021) 1331.
[67] Martina Roso, Carlo Boaretti, Maria Guglielmina Pelizzo, Annamaria Lauria, Michele Modesti, Alessandra Lorenzetti, Nanostructured photocatalysts based on different oxidized graphenes for VOCs removal, Ind. Eng. Chem. Res. 56 (36) (2017) 9980–9992.
[68] Carlo Boaretti, Giuseppe Vitiello, Giuseppina Luciani, Alessandra Lorenzetti, Michele Modesti, Martina Roso, Electrospun active media based on polyvinylidene fluoride (PVDF)-graphene-TiO2 nanocomposite materials for methanol and acetaldehyde gas-phase abatement, Catalysts 10 (9) (2020) 1017.